

# Size Effect of Local Current-Voltage Characteristics of $MX_2$ Nanoflakes: Local Density of States Reconstruction from Scanning Tunneling Microscopy Experiments

Anna N. Morozovska<sup>1,\*</sup>, Hanna V. Shevliakova,<sup>1,2</sup> Yaroslava Yu. Lopatina,<sup>1</sup> Mykola E. Yelisieiev<sup>3</sup>, Galina I. Dovbeshko<sup>1</sup>,<sup>1</sup> Marina V. Olenchuk<sup>1</sup>,<sup>1</sup> George S. Svechnikov<sup>1</sup>,<sup>2</sup> Sergei V. Kalinin,<sup>4,†</sup> Yunseok Kim<sup>5,‡</sup>,<sup>5</sup> and Eugene A. Eliseev<sup>6,§</sup>

<sup>1</sup> Institute of Physics, National Academy of Sciences of Ukraine, 46, pr. Nauky, 03028 Kyiv, Ukraine

<sup>2</sup> Department of Microelectronics, National Technical University of Ukraine “Igor Sikorsky Kyiv Polytechnic Institute”, Kyiv, Ukraine

<sup>3</sup> Taras Shevchenko National University of Kyiv, Volodymyrska Street 64, Kyiv, 01601, Ukraine

<sup>4</sup> Department of Materials Science and Engineering, University of Tennessee, Knoxville, Tennessee 37920, USA

<sup>5</sup> School of Advanced Materials Science and Engineering, Sungkyunkwan University (SKKU), Suwon 16419, Republic of Korea

<sup>6</sup> Institute for Problems of Materials Science, National Academy of Sciences of Ukraine, Krjjanovskogo 3, 03142 Kyiv, Ukraine

(Received 25 January 2022; revised 12 April 2022; accepted 9 May 2022; published 21 June 2022)

Local current-voltage characteristics for low-dimensional transition-metal dichalcogenides (LDTMD), as well as the reconstruction of their local density of states (LDOS) from scanning tunneling microscopy (STM) experiments, are of fundamental interest and can be useful for advanced applications. Most of the existing models either have limited applicability for complex-shaped LDTMDs (e.g., those based on the Simmons approach) or require solving of an ill-defined integral equation to deconvolute the unknown LDOS (e.g., those based on the Tersoff approach). Using a serial expansion of the Tersoff formulas, we propose a flexible method to reconstruct the LDOS from local current-voltage characteristics measured in STM experiments. We establish a set of key physical parameters, which characterize the tunneling current of a STM-probe–sample contact and the sample LDOS expanded in Gaussian functions. Using a direct variational method coupled with probabilistic analysis, we determine these parameters from the STM experiments for  $\text{MoS}_2$  nanoflakes with different numbers of layers. The main result is the reconstruction of the LDOS in a relatively wide energy range around the Fermi level, which allows us to gain insight into the local band structure of LDTMDs. The reconstructed LDOS reveal pronounced size effects for the single-layer, two-layer, and three-layer  $\text{MoS}_2$  nanoflakes, which we relate to the low dimensionality and strong bending or corrugation of the nanoflakes. We hope that the proposed elaboration of the Tersoff approach, allowing LDOS reconstruction, will be of critical interest for the quantitative description of STM experiments and also of use to better understand the microscopic physical aspects of the surface, strain, and bending contributions to the LDTMDs’ electronic properties.

DOI: 10.1103/PhysRevApplied.17.064037

## I. INTRODUCTION

The tunneling effect is widely used in solid-state physics for the spectroscopy of electronic states. The method is based on the dependence of the tunneling current on the number of states that form the tunnel contact in semiconductors over the energy range from 0 to  $eV$ , which is

counted from the Fermi level,  $E_F$ , and  $V$  is the tunneling gap bias. For scanning tunneling microscopy (STM), it is necessary to take into account the coordinate dependence of the local density of states (LDOS), which opens the possibility for scanning tunneling spectroscopy (STS) with high spatial resolution [1].

Local current-voltage ( $I$ - $V$ ) characteristics for low-dimensional (LD) transition-metal dichalcogenides (TMDs), as well as the reconstruction of their LDOS from STM  $I$ - $V$  curves, is of fundamental interest and can be useful for advanced applications, primarily because their semiconducting properties are versatile and tunable [2,3].

\*anna.n.morozovska@gmail.com

†sergei2@utk.edu

‡yunseokkim@skku.edu

§eugene.a.eliseev@gmail.com

For instance, the structural, polar, and electronic properties of low-dimensional  $MX_2$  ( $M$ , metal, Mo, V, W;  $X$ , chalcogen, S, Se, Te) [4,5] and Janus compounds  $MXY$  ( $X, Y$ , chalcogens) [6,7] vary from a nonpolar to a ferroelectric state and from a direct-band semiconductor to metallic conductivity [8,9]. Studies on the LD  $MoX_2$  local electrical conductivity attract much interest [10–12], and the property is readily tunable. In particular, the structural and electronic properties of LD  $MoS_2$  may be different, depending on the preparation conditions, concentration of impurities, and defects [13–16]. The local bending of  $MoX_2$  nanoflakes can lead to a significant dependence of the free carrier concentration on the strain gradient [17–19].

Most existing models for the determination of LDOS from local  $I$ - $V$  curves have limited applicability for complex-shaped LDTMDs, such as bent and/or corrugated nanolayers, nanoflakes, and ultrasmall nanoparticles. In particular, the one-dimensional tunneling-current model, proposed by Simmons [20,21], is *a priori* not applicable to nanoflakes due to the influence of strongly inhomogeneous “transverse” electric fields that can be created by bending flakes and other edge effects. In addition, this model is not applicable to atomically sharp probes. More suitable is the Tersoff approach [22], which is widely used in STS, and potentially allows the determination of the LDOS of the studied substrate at the Fermi level; also, it can be adapted to modern atomically sharp probes and substrate inhomogeneities [1,23]. However, the Tersoff approach [22] requires solving an ill-defined integral equation to deconvolute the unknown LDOS in the finite energy range around the Fermi level. Later on, Koslowski *et al.* [24] proposed a method to recover the LDOS of a sample from STM spectroscopic data based on a numerical solution of the developed Volterra integral equation. This approach was further elaborated by Passoni *et al.* [25], who took different physical effects into consideration, such as the influence of the nonconstant tip LDOS. These and other approaches to the interpretation of STM experimental results were reviewed by Palotás *et al.* [26].

Using a serial expansion of the Tersoff formulas [22], in this work, we propose a method for how to reconstruct the LDOS from the local  $I$ - $V$  curves measured in STM experiments for  $MoS_2$  nanoflakes with different numbers of layers. Below, we explain how to reconstruct the LDOS over a relatively wide energy range around the Fermi level and reveal pronounced size effects for the single-layer, two-layer, and three-layer  $MoS_2$  nanoflakes.

The manuscript is structured as follows. Section II contains the formulation of the problem of LDOS reconstruction from the STM current and analytical expressions for the tunneling current derived for LDOS expanded in Gaussian functions. Section III provides an analysis of the local  $I$ - $V$  curves measured by STM in single-layer, two-layer, and three-layer  $MoS_2$  nanoflakes, and the reconstruction

of the LDOS from these curves. Section IV is a brief summary. Calculation details and auxiliary figures are listed in the Supplemental Material [27].

## II. MODELING OF THE TUNNELING CURRENT AND LDOS OF $MoS_2$ NANOFOLAKES

Typical STM images of  $MoS_2$  nanoflakes on HOPG and the surface topography along the  $A$ - $B$  direction are shown in Figs. 1(a) and 1(b). STM images of different parts of the samples are obtained for  $MoS_2$  nanoflakes of arbitrary shape and size.

It is shown in Ref. [28] that bulk  $MoS_2$  is an indirect-band semiconductor with a band gap of 1.2 eV, which begins at point  $\Gamma$  and ends at the bottom of the conduction band, halfway between points  $\Gamma$  and  $K$ . As the number of layers decreases, the main indirect band gap (from point  $\Gamma$  to the middle between point  $\Gamma$  and point  $K$ ) increases due to a quantum constraint and becomes larger than the direct band gap located at point  $K$  in the case of a  $MoS_2$  monolayer. Within a flat monolayer,  $MoS_2$  is transformed from a bulk nonindirect semiconductor into a two-dimensional straight-band semiconductor with a larger band gap. The indirect band gap of bulk  $MoS_2$  (1.2 eV) is replaced by a direct band gap (1.9 eV) at point  $K$  of monolayer  $MoS_2$ . The local strains, large strain gradients, bending, and especially corrugation can strongly affect the DOS of  $MoS_2$  nanoflakes, making them semimetallic or metallic in the  $1T'$  phase [7,8,17–19]. To probe the influence of strain, we used strongly deformed nanoflakes. The strong deformation of the studied nanoflakes is clearly visible from a typical SEM image in Fig. 1(c).

Using multidimensional tunneling-current models [29] and perturbation theory, the tunneling current,  $I$ , through the space between the sample and the probe can be written as

$$I(x, y) = \frac{2\pi e}{\hbar} \sum_{\mu\nu} f(E_\mu)[1 - f(E_\nu + eV)] |M_{\mu\nu}(x, y)|^2 \delta(E_\mu - E_\nu), \quad (1a)$$

where  $f(E) = 1/(1 + \exp((E - E_F)/k_B T))$  is the Fermi function;  $E_F$  is the Fermi level; and  $eV$  is the applied voltage, which may depend on the “transverse” surface relief. The matrix element,  $M_{\mu\nu}$ , is

$$M_{\mu\nu} = -\frac{\hbar^2}{2m} \int (\psi_\mu^* \nabla \psi_\nu - \psi_\nu^* \nabla \psi_\mu) ds, \quad (1b)$$

between the undisturbed states of the probe  $\psi_\mu$  and the sample surface  $\psi_\nu$ ;  $E_\mu$  is the energy of state  $\psi_\mu$  without tunneling. Integration is carried out on any surface  $S$  in the air-vacuum gap between the probe and the surface. According to perturbation theory, these wave functions satisfy the stationary Schrödinger equation,

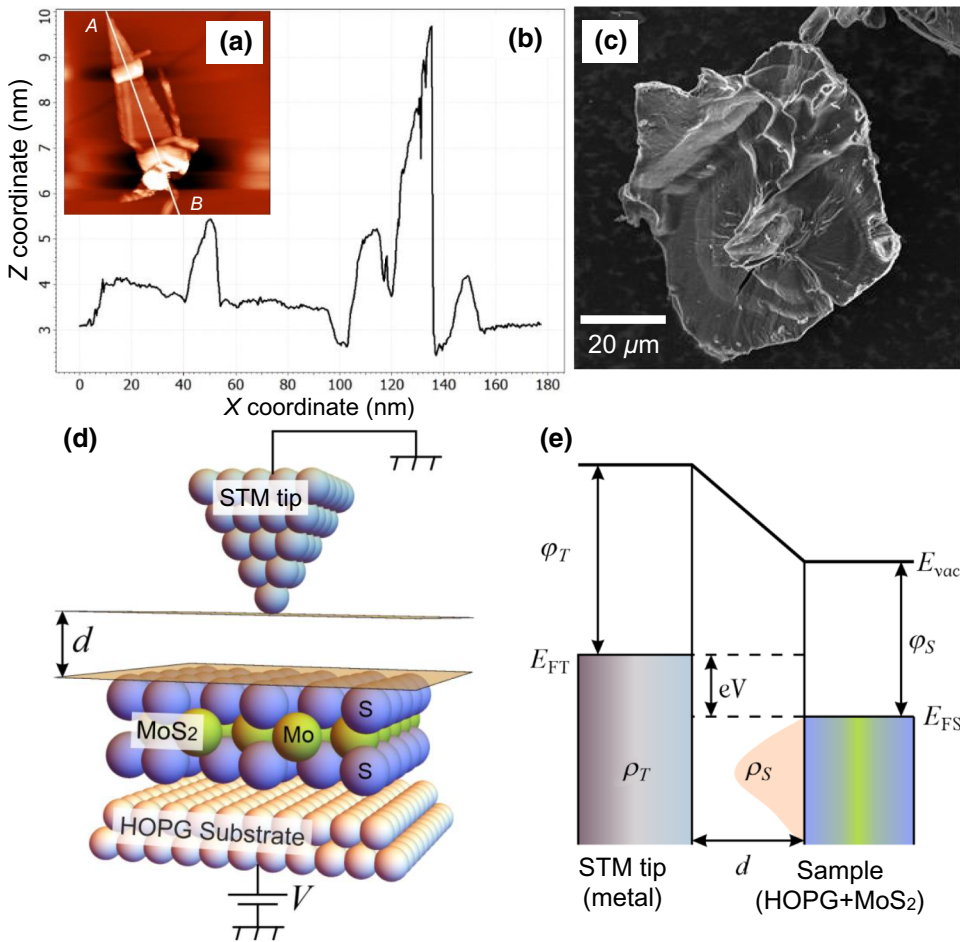


FIG. 1. (a) “Sparking” and corrugated nanoflake placed between the STM tip and conducting HOPG substrate. (b) Surface topography along the *A*-*B* direction. (c) SEM image of a corrugated single-layer MoS<sub>2</sub> nanoflake. Schematics of STM experiment (d) and zone scheme (e) used in our calculations.

$-(\hbar^2/2m)\Delta\psi + e(V_S + V_T)\psi = E\psi$ , where the potential,  $V_T$ , which is created by the STM probe, is considered to be a small perturbation in comparison with the potential of the sample surface,  $V_S$ . Summation in Eq. (1a) is conducted on all possible electronic states (see Appendix A within the Supplemental Material for details [27]).

When performing STM studies on semiconductor samples, the applied voltage,  $V$ , can reach (0.5–2) V, which is significant compared to  $k_B T$  at room temperature (26 meV). At such voltages, the local densities of the probe and substrate states can still be introduced, but the point-probe approximation, which is valid at very low voltages of about (1–10) mV, cannot be used. Under these conditions, Eq. (1a) can be roughly written in the following form [30]:

$$I(\mathbf{r}, V) \cong \frac{4\pi e}{\hbar} \int_{E_F}^{E_F+eV} \rho_T(E + eV) \tilde{\rho}_S(\mathbf{r}, E) T(\mathbf{r}, E, V) dE, \quad (2)$$

where  $\rho_T(E + eV)$  is the LDOS related to the probe,  $\tilde{\rho}_S(\mathbf{r}, E)$  is the LDOS related to the sample in point  $\mathbf{r}$ , and  $T(\mathbf{r}, E, V) = |M|^2$  is the local probability of electron tunneling. Notably, if LDOS has a singularity at the Fermi

energy,  $E = E_F$ , the value of  $I(\mathbf{r}, 0)$  is nonzero and determined by the surface states [30], work-function difference, and/or Schottky barriers. For the purposes of correct fitting, we separate  $I(\mathbf{r}, 0) \equiv I_S$  and introduce the “regular” part of the sample LDOS denoted as  $\rho_s(\mathbf{r}, E)$ .

Within the Wentzel-Kramers-Brillouin (WKB) approximation, the value of the barrier transparency coefficient,  $T(\mathbf{r}, E, eV)$ , is given by [1]

$$T(\mathbf{r}, E, V) = \exp[-2\kappa d] \cong \exp \left[ -2d \sqrt{\frac{2me}{\hbar^2} \left( \frac{\varphi_T + \varphi_S}{2} - E + \frac{V}{2} \right)} \right], \quad (3a)$$

where  $d$  is the probe-sample distance, which can vary during scanning (e.g., in dc mode), and  $\kappa$  is a damping constant. Equation (3a) is based on the assumption that only the  $s$  functions of the probe make a major contribution to its LDOS near the Fermi level,  $\rho_T(E_F)$ , which is proportional to  $|\psi_\mu|^2 \sim \exp(-2\kappa d)$ . The damping constant is given by

$$\kappa = \sqrt{\frac{2me}{\hbar^2} \left( \frac{\varphi_T + \varphi_S}{2} - E + \frac{V}{2} \right)}, \quad (3b)$$

where  $\varphi_T$  and  $\varphi_S$  are the work functions of the electron at the surface of the probe and at the sample surface, respectively. Hereinafter, we measure them in voltage units.

If the sample LDOS,  $\rho_s(\mathbf{r}, E)$ , is dominated in the spectrum, and the probe states,  $\rho_T$ , are stable, Eq. (2) can be simplified as

$$\begin{aligned} I(\mathbf{r}, V) \cong I_S + \frac{4\pi}{\hbar} \rho_T \int_0^V \rho_s(\mathbf{r}, E + E_F) \\ \times \exp \left[ -2d \sqrt{\frac{2me}{\hbar^2} \left( \frac{\varphi_T + \varphi_S}{2} - E_F - E + \frac{V}{2} \right)} \right] \\ \times dE. \end{aligned} \quad (4)$$

The “residual” current,  $I_S$ , is related to the LDOS peculiarity at  $E = E_F$  in Eq. (2). All energies in Eq. (4) are written in voltage units, and the condition  $(\varphi_T + \varphi_S)/2 - E_F - E + (V/2) \geq 0$  should be valid.

Equation (4) is suitable for the deconvolution of the sample LDOS with STS maps. Since a tunneling current is measured with a significant error, it makes sense to deconvolve it using a direct-variation method, similar to that for piezoresponse force spectroscopy [31].

The tunneling-current values,  $I_n(\mathbf{r})$ , are measured for voltages of  $V_n$ , where  $n = 1, \dots, N$ . For each scan point  $\mathbf{r}$ , we need to find the parameters of the transparency coefficient,  $T(\mathbf{r}, E, eV)$ , and the DOS  $\rho_s(\mathbf{r}, E)$ , which minimize the following functional:

$$\mathcal{Q}(\mathbf{r}) = \frac{1}{N} \sum_{n=1}^N [I_n(\mathbf{r}) - I(\mathbf{r}, V_n)]^2. \quad (5)$$

From Eq. (4), the parameters are the probe-sample distance,  $d$ ; the voltage shift,  $V_S$ ; the sum of the work functions,  $\phi = (\varphi_T + \varphi_S)/2$ ; and the sample LDOS,  $\rho_s(\mathbf{r}, E)$ , the form of which is *a priori* unknown but may depend significantly on the number of MoS<sub>2</sub> layers and the local electric fields, which “distort” it. The selection of the form of this function and its parameters is the main purpose of the model. We need to go through several case studies and choose the most appropriate results. Below, we use the sum of several Gaussian functions, which can model the well-localized LDOS of various types:

$$\rho_s(\mathbf{r}, E) = \sum_{m=1}^N g_m \exp \left[ -\frac{(E - E_F - E_m)^2}{\Delta_m^2} \right]. \quad (6a)$$

Here, the number  $N$  and the fitting parameters, such as the number of states,  $g_m$ ; the maximum positions of the corresponding DOS,  $E_m$ ; and their dispersions,  $\Delta_m$ , can be defined from STM data using Eq. (5) and, e.g., standard numerical packages based on conventional Gaussian

fits [32]. The Fermi energy,  $E_F$ , is determined by the band structure of the tip-gap-sample-substrate system. Below, we omit the argument “ $\mathbf{r}$ ” in  $\rho_s(\mathbf{r}, E)$  for the sake of simplicity.

First of all, one should try to optimize (in fact, to minimize) the number  $N$  to reach an appropriate accuracy of fitting without including extra terms in Eq. (6a), which could be artifacts rather than have physical meaning. Use of the series in Eq. (6a) can only be rigorous enough for a well-localized LDOS, and this limitation is assumed to be valid hereinafter for LDTMDs. In other words, Eq. (6a) with a minimal number  $N$  (e.g.,  $1 \leq N \leq 5$ ) “captures” only the central part of the real LDOS around the Fermi level, while its possible “tails” cannot be determined by the method. Let us underline that other methods of LDOS reconstruction [24–26] should be used in all questionable cases and especially for LDOS delocalization, and the most efficient should be selected. The general case is out of the scope of this work.

For model cases of an intrinsic *p*-type or *n*-type semiconductor, semimetal, or metal with a simple well-localized LDOS, it is enough to regard that  $1 \leq N \leq 2$ , and remove the first terms from the series in Eq. (6a):

$$\begin{aligned} \rho_s(E) = g_e \exp \left[ -\frac{(E - E_F - E_e)^2}{\Delta_e^2} \right] \\ + g_p \exp \left[ -\frac{(E - E_F + E_p)^2}{\Delta_p^2} \right]. \end{aligned} \quad (6b)$$

The LDOS in Eq. (6b) contain only six fitting parameters: the number of electron and hole states,  $g_e$  and  $g_p$ ; the maximum positions of the corresponding DOS,  $E_e$  and  $E_p$ ; and their dispersions,  $\Delta_e$  and  $\Delta_p$ . For the impurity-free case,  $g_e = g_p$ ,  $\Delta_e = \Delta_p = \Delta$ , and  $E_e = E_p = E_s$ . The standard automated fitting procedures can unambiguously resolve these cases if  $|E_s| \geq \Delta/\sqrt{3}$ . Sketches of the LDOS calculated from Eq. (6b) for several ratios of  $|E_s|/\Delta$  are shown by curves 1, 2, and 3 in Fig. 2. The case of  $g_e \gg g_p$  (including the case of  $g_p = 0$ , and so,  $N = 1$ ) corresponds to *n*-type doping, and  $g_e \ll g_p$  (including the case of  $g_e = 0$ , and so,  $N = 1$ ) is valid for *p*-type doping.

Despite Eq. (6b) having a limited applicability range, it can describe the special cases that we are primarily interested in. Specifically, for flat and weakly deformed areas of multilayer MoS<sub>2</sub> nanoflakes, their LDOS may be close to a proper semiconductor with a well-separated band gap, i.e.,  $g_e \cong g_p$ ,  $\Delta_e = \Delta_p = \Delta$ ,  $E_e = E_p = E_s$ , and  $|E_s| \geq 3\Delta$ . Using the results obtained by the authors of Ref. [28], it can be assumed that, for strongly bent sections of corrugated MoS<sub>2</sub> nanoflakes, the LDOS are similar to those of a semimetal or even metal in the 1T phase. This means that the LDOS of the electron and hole overlap, and so we can assume  $g_e \sim g_p$  and  $\Delta/\sqrt{3} \leq |E_s| \leq \sqrt{3}\Delta$  in this case.

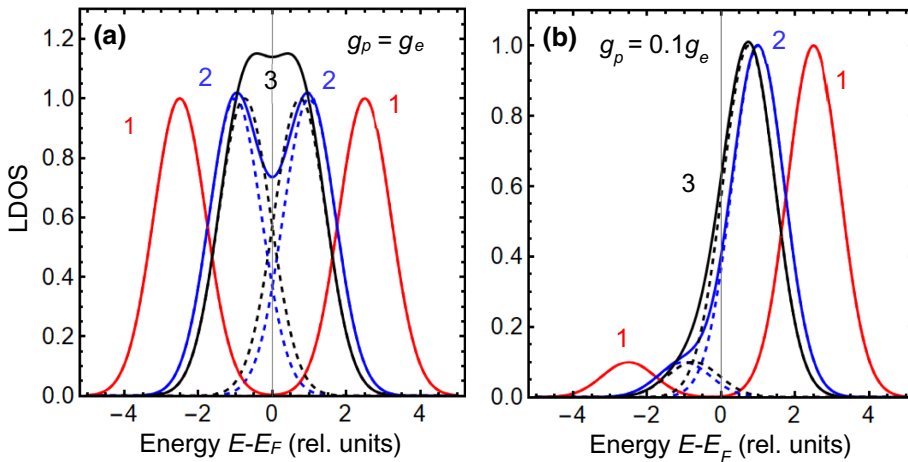


FIG. 2. Red, blue, and black curves illustrate LDOS calculated from Eq. (6b) for parameters  $E_s = 2.5\Delta$  (curves 1),  $E_s = \Delta$  (curves 2), and  $E_s = 0.75\Delta$  (curves 3),  $g_e = g_p$  (a) and  $g_e = 0.1g_p$  (b). For all curves,  $\Delta_e = \Delta_p = \Delta$  and  $E_e = E_p = E_s$ . Dashed curves show the contribution of two Gaussians to solid curves 2 and 3.

For a metallic *n*-type MoS<sub>2</sub> and/or electron-conducting substrate, the LDOS is maximal at the Fermi energy, so  $g_e \gg g_p$  (including the case of  $g_p \rightarrow 0$ ). For the *p* type, we have  $g_e \ll g_p$  (including the case of  $g_e \rightarrow 0$ ). The problem with parameter determination appears at  $|E_{e,p}| \leq \Delta_{e,p}/\sqrt{3}$  and  $g_e \cong g_p$ , and, naturally, it does not appear in the case of  $g_e = 0$  (or  $g_p = 0$ ) at arbitrary ratio  $|E_e/\Delta_e|$  (or  $|E_p/\Delta_p|$ ) since  $N = 1$  in Eq. (6a) in this case. So, it makes sense to limit potential fitting by two simple cases.

Case study (a), to regard  $\Delta_e = \Delta_p = \Delta$  and  $E_e = E_p = E_s$  and vary the parameter  $|E_s|$  in the range  $\Delta/\sqrt{3} \leq |E_s| \leq \sqrt{3}\Delta$  and the ratio  $(g_e - g_p)/(g_e + g_p)$  in the range  $0 < |(g_e - g_p)/(g_e + g_p)| < 1$  [when  $N = 2$  in Eq. (6a)].

Case study (b), to consider the special case,  $N = 1$ , corresponding to  $g_e = 0$  (or  $g_p = 0$ ) without any restrictions on the ratio  $|E_e/\Delta_e|$  (or  $|E_p/\Delta_p|$ ).

The restrictive division on case studies (a) and (b) allows us to exclude the “unresolved” region of parameters in Eq. (6b),  $|E_{e,p}| \leq \Delta_{e,p}/\sqrt{3}$  and  $g_e \cong g_p$ , from the iteration procedure and to select the best fitting corresponding to either  $N = 1$  or  $N = 2$  in the actual parameter space, depending on overlap of the electron and hole states.

Prior to applying the results of the case studies to Eq. (6), we expand the tunneling current of Eq. (4) in the Taylor series with respect to the voltage powers:

$$I(V) \cong I_S + \sum_{i=1}^n \sigma_i V^i, \quad (7a)$$

where  $n$  is an integer, and the offset current,  $I_S$ , can be related to several factors, including instrumental errors (e.g., the leakage current at the current amplifier). To avoid artifacts, it makes sense to subtract the bias current value from the  $I$ - $V$  curves and subsequently analyze only the difference to determine the fitting parameters  $\sigma_i$  in Eq. (7a).

The first-five expansion coefficients,  $\sigma_i$ , are given by

$$\sigma_1 = \rho e^{-\sqrt{Z\phi}} \rho_s(E_F), \quad (7b)$$

$$\sigma_2 = \frac{\rho}{2} e^{-\sqrt{Z\phi}} \left. \frac{\partial \rho_s(E)}{\partial E} \right|_{E \rightarrow E_F}, \quad (7c)$$

$$\sigma_3 = \frac{\rho}{6} e^{-\sqrt{Z\phi}} \left[ \frac{Z\phi + \sqrt{Z\phi}}{16\phi^2} \rho_s(E) + \frac{1}{4} \sqrt{\frac{Z}{\phi}} \frac{\partial \rho_s(E)}{\partial E} + \frac{\partial^2 \rho_s(E)}{\partial E^2} \right] \Big|_{E \rightarrow E_F}, \quad (7d)$$

$$\sigma_4 = \frac{\rho}{24} e^{-\sqrt{Z\phi}} \left[ \frac{Z\phi + \sqrt{Z\phi}}{8\phi^2} \frac{\partial \rho_s(E)}{\partial E} + \frac{1}{2} \sqrt{\frac{Z}{\phi}} \frac{\partial^2 \rho_s(E)}{\partial E^2} + \frac{\partial^3 \rho_s(E)}{\partial E^3} \right] \Big|_{E \rightarrow E_F}, \quad (7e)$$

$$\begin{aligned} \sigma_5 = \frac{\rho}{120} e^{-\sqrt{Z\phi}} & \left[ \frac{15Z\phi + Z^2\phi^2 + 15\sqrt{Z\phi} + 6(Z\phi)^{3/2}}{256\phi^4} \rho_s(E) + \frac{3Z\phi + 3\sqrt{Z\phi} + (Z\phi)^{3/2}}{32\phi^3} \frac{\partial \rho_s(E)}{\partial E} \right. \\ & \left. + \frac{Z\phi + \sqrt{Z\phi}}{4\phi^2} \frac{\partial^2 \rho_s(E)}{\partial E^2} + \frac{3\sqrt{Z\phi}}{4\phi} \frac{\partial^3 \rho_s(E)}{\partial E^3} + \frac{\partial^4 \rho_s(E)}{\partial E^4} \right] \Big|_{E \rightarrow E_F}, \end{aligned} \quad (7f)$$

where we introduce the factor  $Z = (8em/\hbar^2)d^2$ , which is proportional to the second power of the tip-sample separation,  $d$ ; the barrier height,  $\phi = ((\varphi_T + \varphi_S)/2) - E_F$ ; and the tip LDOS magnitude,  $\rho = (4\pi/\hbar)\rho_T$ .

It may seem that Eq. (7), based on a Taylor-series expansion of classical tunneling current in Eq. (4) about zero bias, is valid for arbitrary LDOS. Here, the first expansion coefficient,  $\sigma_1$ , contains information about the sample LDOS at the local Fermi level,  $\rho_s(E_F)$ ; the second and other coefficients contain a mixture of information about the LDOS and their derivatives,  $\partial^i \rho_s(E)/\partial E^i$  at  $E \rightarrow E_F$ . Equation (7) attempts to reconstruct the whole LDOS curve,  $\rho_s(E)$ , from its  $n$  derivatives at zero voltage. The attempt has several limitations.

First, the polynomial expansion, Eq. (7a), would necessarily diverge at energies far from  $E_F$ . Below, we try to overcome the divergency by restricting the series expansion to the well-localized Gaussians in Eq. (6a), where the derivatives in Eqs. (7b)–(7f) are evaluated at  $E \rightarrow E_F$ , and the fitting of STM curves is used to estimate the Gaussian parameters. Next, one should realize that the double-Gaussian assumption limits the validity range of the series expansion approach, as discussed for Eq. (6b).

Second, the case of a semiconductor with well-separated electron and hole bands far from  $E_F$ , modeled by a widely spaced double Gaussian with  $|E_s| \geq 3\Delta$  (see, e.g., red curves 1 in Fig. 2), corresponds to zero density of states at the Fermi level; its derivatives are very small at  $E \rightarrow E_F$  and become experimentally indistinguishable from zero at  $|E_s| \gg 3\Delta$ . For the latter case, one cannot reconstruct the LDOS based on a Taylor-series expansion, Eq. (7), taken at the Fermi energy,  $E \rightarrow E_F$ . For the gapped semiconductor, one should directly substitute the double-Gaussian LDOS, Eq. (6b), into Eq. (4) and determine the fitting parameters by the variational method in the double-Gaussian parameter space. However, the correct realization of this direct way appears to be much more complex and less reliable

in comparison with the use of Eqs. (7b)–(7f), because the corresponding  $I$ - $V$  curves (either simulated or real experimental data) contain a wide region of zero current around  $|V| < V_b$  followed by a sharp increase of the tunnel current at  $|V| > V_b$ . The sharp increase or “opening” occurs at high voltage,  $V_b \geq (1 - 3)$  V and is usually accompanied by irregular jumps and a significant difference between the forward and backward directions of the  $I$ - $V$  curves related to high uncertainty (a typical example is shown in Appendix C within the Supplemental Material [27]). The sharp opening at high voltages and irregular jumps do not allow us to estimate reliably (i.e., with small errors) the double-Gaussian curve parameters from the  $I$ - $V$  curves using the direct algorithm. Based on the discussion, the fitting most probably fails for the widely spaced double Gaussian, but can succeed in other cases (e.g., as shown by curves 2 and 3 in Fig. 2).

In addition to the above limitations, we should underline that the system in Eq. (7), written for  $n$  coefficients,  $\sigma_n$ , contains  $n$  unknown characteristics of the sample LDOS,  $\rho_s(E_F)$ ,  $\partial \rho_s(E_F)/\partial E$ , ...,  $(\partial^{n-1} \rho_s(E_F))/\partial E^{n-1}$ , and three unknown parameters of the tip, tunneling gap, and contact,  $\rho$ ,  $Z$ , and  $\phi$ , respectively, which are included as combinations of  $\rho e^{-\sqrt{Z}\phi}$ ,  $Z\phi$ , and  $1/\phi$ . Since the system of  $n$  equations contains  $(n+3)$  unknown variables, it is ill defined for the unique reconstruction of the Tailor series:

$$\rho_s(E) = \rho_s(E_F) + \sum_{n=1}^{\infty} \frac{\partial^n \rho_s(E_F)}{\partial E^n} \frac{(E - E_F)^n}{n!},$$

for arbitrary  $\rho_s(E)$ . To approximately solve the ill-defined problem, we need to use an estimation for  $\rho_s(E)$ , significantly reducing the number of unknown parameters in  $\rho_s(E)$ .

For the LDOS from Eq. (6b), the first expansion coefficients,  $\sigma_i$ , are given by

$$\sigma_1 = \rho(g_e + g_p) \exp \left[ -\sqrt{Z\phi} - \frac{E_s^2}{\Delta^2} \right], \quad (8a)$$

$$\sigma_2 = \rho(g_e - g_p) \frac{E_s}{\Delta^2} \exp \left[ -\sqrt{Z\phi} - \frac{E_s^2}{\Delta^2} \right], \quad (8b)$$

$$\sigma_3 = \frac{\rho}{6} \exp \left[ -\sqrt{Z\phi} - \frac{E_s^2}{\Delta^2} \right] \left[ \frac{Z\phi + \sqrt{Z\phi}}{16\phi^2} (g_e + g_p) + \frac{1}{2} \sqrt{\frac{Z}{\phi}} (g_e - g_p) \frac{E_s}{\Delta^2} + 2(g_e + g_p) \frac{2E_s^2 - \Delta^2}{\Delta^4} \right], \quad (8c)$$

$$\sigma_4 = \frac{\rho}{24} \exp \left[ -\sqrt{Z\phi} - \frac{E_s^2}{\Delta^2} \right] \left[ \frac{Z\phi + \sqrt{Z\phi}}{4\phi^2} (g_e - g_p) \frac{E_s}{\Delta^2} + \sqrt{\frac{Z}{\phi}} \frac{2E_s^2 - \Delta^2}{2\Delta^4} (g_e + g_p) + 4 \frac{2E_s^2 - 3\Delta^2}{\Delta^4} \frac{E_s}{\Delta^2} (g_e - g_p) \right]. \quad (8d)$$

$$\sigma_5 = \frac{\rho}{120} \exp \left[ -\sqrt{Z\phi} - \frac{E_s^2}{\Delta^2} \right] \left[ \frac{15Z\phi + (Z\phi)^2 + 15\sqrt{Z\phi} + 6(Z\phi)^{3/2}}{256\phi^4} (g_e + g_p) + \frac{3Z\phi + 3\sqrt{Z\phi} + (Z\phi)^{3/2}}{16\phi^3} (g_e - g_p) \frac{E_s}{\Delta^2} \right. \\ \left. + \frac{Z\phi + \sqrt{Z\phi}}{2\phi^2} \frac{2E_s^2 - \Delta^2}{\Delta^4} (g_e + g_p) + 3\sqrt{\frac{Z}{\phi}} \frac{2E_s^2 - 3\Delta^2}{\Delta^4} (g_e - g_p) \frac{E_s}{\Delta^2} + 4 \frac{4E_s^2(E_s^2 - 3\Delta^2) + 3\Delta^4}{\Delta^8} (g_e + g_p) \right]. \quad (8e)$$

The system in Eq. (8) written for  $n$  coefficients,  $\sigma_n$ , contains four unknown characteristics of the sample LDOS,  $g_e$ ,  $g_p$ ,  $E_s$ , and  $\Delta^2$ , and three unknown parameters of the tip-sample contact,  $\rho$ ,  $Z$ , and  $\phi$ . Therefore, rigorously, we need seven experimental values of  $\sigma_1 - \sigma_7$  for fitting. However, the accuracy of the polynomial fitting of the local  $I$ - $V$  curves in the range of small voltages may not allow the determination of so many coefficients  $\sigma_i$  without significant noise-related errors. For instance, for STM data considered in the next section, only the first 4–5 coefficients  $\sigma_i$  can be reliably extracted from data. This noise-related problem forces us to use probabilistic analysis for the determination of the unknown LDOS.

By equating expressions in Eq. (8) for the coefficients  $\sigma_i^{(j)}$ , as determined from the fitting of the STM current  $\sigma_i^{\text{exp}}$ , we can extract the unknown parameters of the nanoflake's effective LDOS. Using the probability analysis

(Bayesian formula), we obtain the following system of equations for the determination of  $P_j$ :

$$\sigma_i^{\text{exp}} = \sum_{j=1}^2 P_j \sigma_i^{(j)}, \quad \sum_{j=1}^2 P_j = 1, \quad 0 \leq P_j \leq 1. \quad (9)$$

The probabilities,  $P_j$ , of *a priori*  $j$ th estimation realization, along with corresponding LDOS parameters, can be determined. Notably, the Bayesian analysis is successfully used for atomically resolved scanning transmission electron microscopy data [33].

### III. DETERMINATION OF THE DOS PROPERTIES FROM STM EXPERIMENTS

Measured by STM, local  $I$ - $V$  curves of a HOPG substrate without nanoflakes are shown in Fig. 3(a). Local  $I$ - $V$

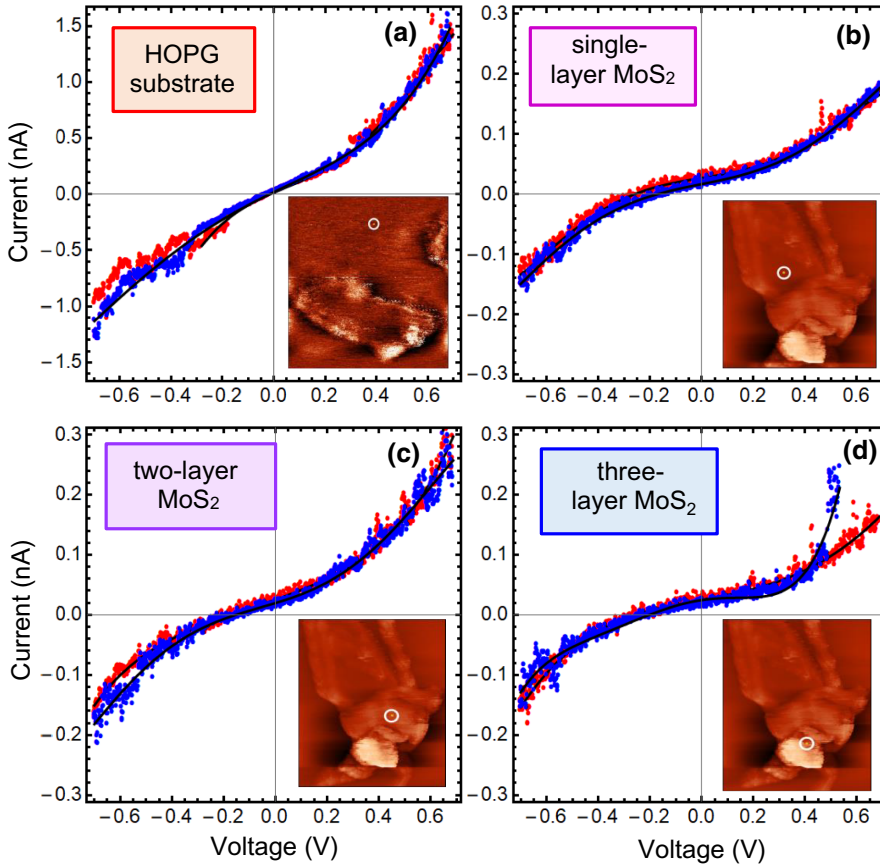


FIG. 3. Local  $I$ - $V$  curves measured in the forward (red symbols) and backward (blue symbols) directions, and their fitting with Eq. (8) (black curves).  $I$ - $V$  curves are measured by STM in the middle of the white circle of the HOPG substrate (a), single-layer, two-layer, and three-layer  $\text{MoS}_2$  nanoflakes of thickness  $h \approx 0.63$  nm (b),  $h \approx 1.21$  nm (c), and  $h \approx 2.03$  nm (d), respectively.

curves for single-layer, two-layer, and three-layer MoS<sub>2</sub> nanoflakes of thickness  $h \approx 0.63$  nm,  $h \approx 1.21$  nm, and  $h \approx 2.03$  nm are shown in Figs. 3(b), 3(c), and 3(d), respectively.

The local  $I$ - $V$  curves are measured at different moments in time at the points on the nanoflake marked with a white circle in the insets in Fig. 3. We also collect 20 curves in the forward (red symbols) and backward (blue symbols) directions. We sweep the voltage forward and record the current, then sweep it backward, making multiple round trips. The variability of the local  $I$ - $V$  curves, the difference between forward and backward sweeps, and the typical jumps in them indicate that the randomness of a particular path of tunneling current can be associated with drift—the local inhomogeneity of electrical conductivity near the surface of MoS<sub>2</sub> nanoflakes—the evolution of which is most likely caused by changes in shape and dynamic deformation during the flow of current. The charge in the inhomogeneity of electrical conductivity is bipolar, as can be seen from the local  $I$ - $V$  curves. However, we cannot explain why the discrepancy for the HOPG substrate is also high, despite the voltage changing between  $-0.5$  and  $+0.5$  V [the vertical scale in Fig. 3(a) is different from those in Figs. 3(b)–3(d)], and we also cannot explain why the difference between forward and backward spectra is most pronounced in the three-layer sample [Fig. 3(d)], which is counterintuitive

because the STM tip is positioned in the most homogenous region, making drift minimal.

It can be seen from Fig. 3 that the forward and backward local  $I$ - $V$  curves are well fitted by Eq. (8) (black curves). Notably, we subtract the zero-bias current value,  $I_S$ , from the  $I$ - $V$  curves and subsequently analyze only the difference to determine the fitting parameters  $\sigma_i$  in Eq. (7a). Thus, the value of  $I_S$  does not affect the procedure for determining the local DOS from the current-voltage characteristics of the tunnel current. We are especially interested in the dependences of the fitting parameters  $\sigma_i$  on the thickness,  $h$ , of the MoS<sub>2</sub> nanoflakes, which can be interpreted as a size effect. Below, we use  $h = Nh_S$ , where  $N = 0, 1, 2$ , and  $3$  and  $h_S \approx 0.63$  nm is the thickness of single-layer MoS<sub>2</sub>.

The dependence of the offset  $I_s$ , voltage shift  $V_s$ , and fitting parameters  $\sigma_i$  on the number,  $N$ , of MoS<sub>2</sub> layers is shown in Fig. 4. The residual value of the tunneling current  $I_s(N)$  decreases by more than 2 times as  $N$  increases from 0 to 3 for the backward run and increases less than 2 times for the forward run [comparing red and blue curves in Fig. 4(a)]. The dependences of  $I_s(N)$  are nonmonotonic and slightly different for the forward and backward directions (“run”) of the  $I$ - $V$  curves. The highest error bars are for  $N = 0$ , corresponding to the HOPG substrate, while the errors are relatively small for  $N = 1 – 3$ .

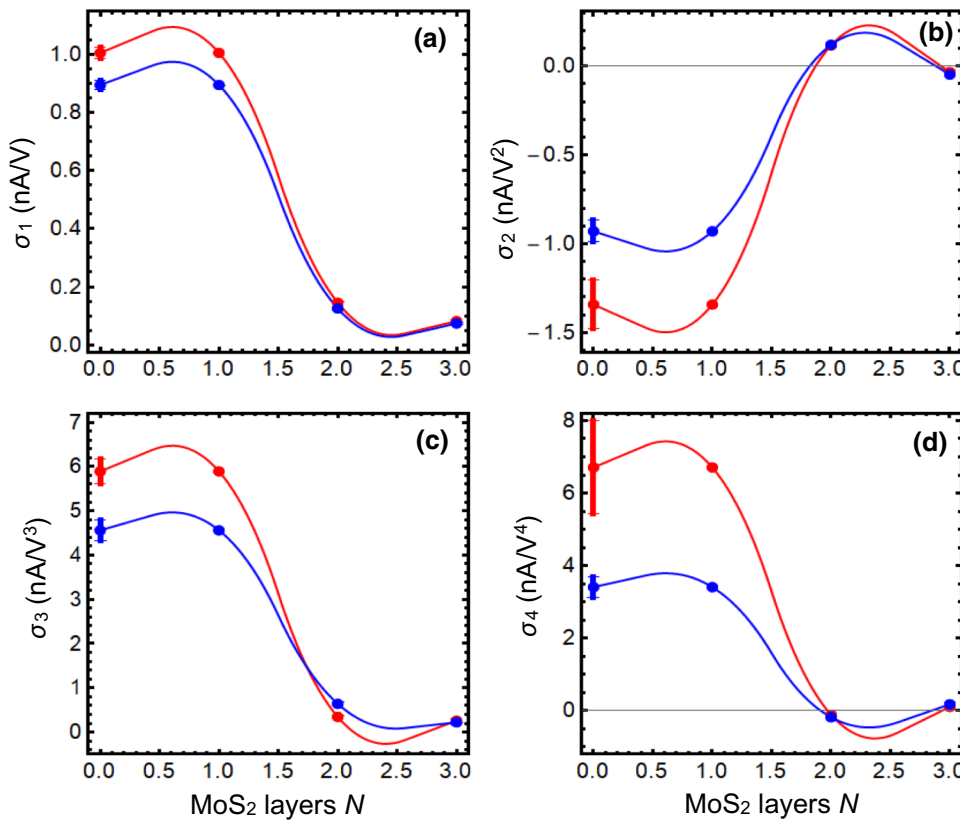


FIG. 4. Dependence of fitting parameters  $\sigma_i$  (a)–(d), on the number,  $N$ , of MoS<sub>2</sub> layers (0, 1, 2, and 3) extracted for the forward (red symbols) and backward (blue symbols) local  $I$ - $V$  curves of MoS<sub>2</sub> nanoflakes on HOPG substrate, as shown in Fig. 3. Solid red and blue curves are spline interpolations.

The voltage shift,  $V_s$ , is always negative, and its absolute value decreases significantly from very small values of about  $-0.01$  to  $-0.25$  V as  $N$  increases from 0 to 1, then  $|V_s|$  decreases for  $N = 2$  and increases again for  $N = 3$  [see Fig. 4(b)]. The nonmonotonic dependences of  $V_s(N)$  are similar for both backward and forward runs. Allowing for the error bars for  $N = 0$ , the size dependences of the odd coefficients,  $\sigma_1(N)$  and  $\sigma_3(N)$ , are quasi-monotonic; they decrease from relatively high positive values ( $1 \text{ nA/V}$  and  $6 \text{ nA/V}^3$ , respectively) to very small positive values as  $N$  increases from 0 to 1 [comparing Figs. 4(c) and 4(e)]. Allowing for the error bars for  $N = 0$ , the size dependences of the even coefficients,  $\sigma_2(N)$  and  $\sigma_4(N)$ , are also quasi-monotonic, but their signs are different; they decrease from relatively high negative (or positive) values to very small negative (or positive) values as  $N$  increase

from 0 to 1 [comparing Figs. 4(d) and 4(f)]. The functional form and values of the dependences of  $\sigma_i(N)$  are similar for both backward and forward runs. It is important to mention that the higher coefficients,  $\sigma_6(N)$  and  $\sigma_7(N)$ , appear to be 0 within the accuracy of experimental error. Therefore, their formal inclusion to determine the LDOS parameters is not required.

Since the size dependences of the fitting parameters,  $\sigma_i(N)$ , are regular, their functional form and values are similar for both backward and forward runs of the local  $I$ - $V$  curves, and therefore, we have an opportunity to determine accurately (“deconvolute”) the parameters of the LDOS of HOPG and MoS<sub>2</sub> nanoflakes given by, e.g., Eq. (6a) using data shown in Fig. 4.

To make the deconvolution procedure more reliable, hereinafter, we introduce positive dimensionless

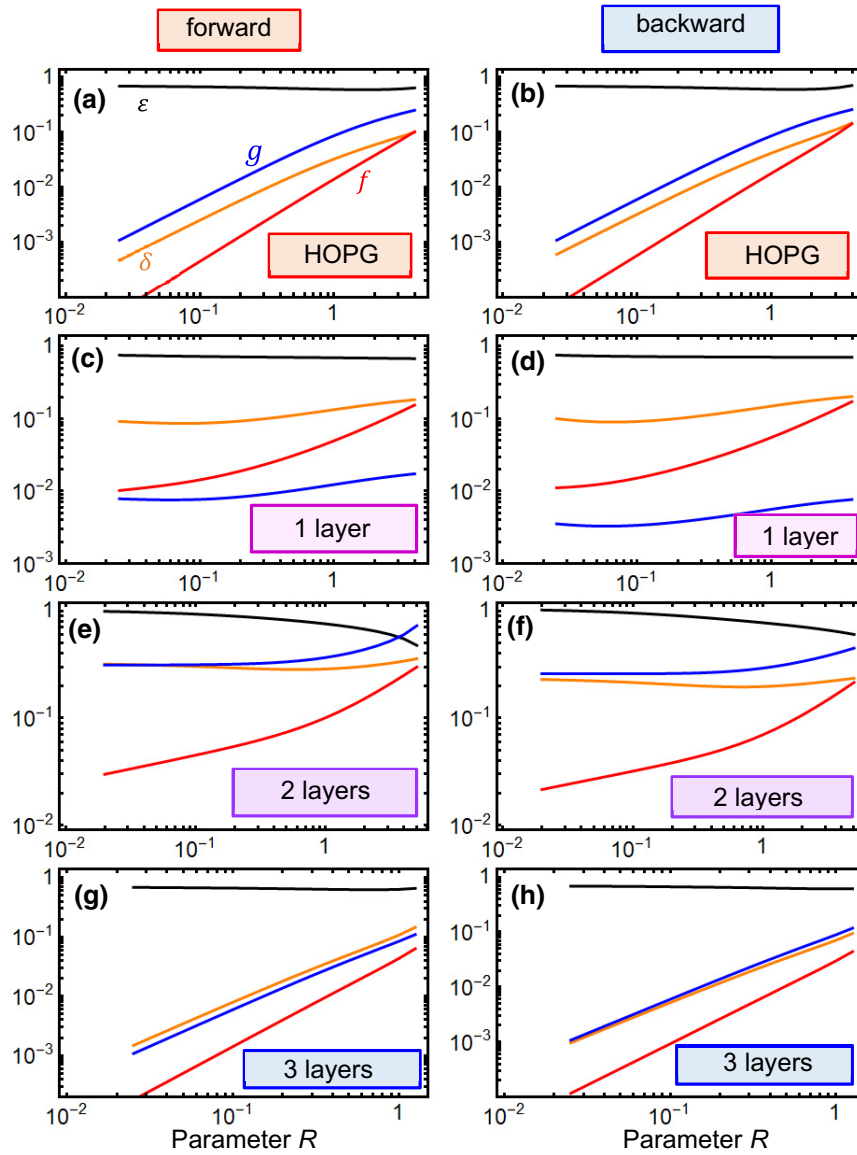


FIG. 5. Dependence of dimensionless fitting parameters  $g$  (blue curves),  $f$  (red curves),  $\delta$  (orange curves), and  $\varepsilon$  (black curves) on parameter  $R$  calculated for HOPG substrate (a, b) and single- (c, d), two- (e, f), and three-layered (g, h) MoS<sub>2</sub> nanoflakes on the HOPG substrate. Plots correspond to the forward (a, c, e, g) and backward (b, d, f, h) local  $I$ - $V$  curves of MoS<sub>2</sub> on HOPG substrate, as shown in Fig. 3.

parameters, which determine the Gaussian-type LDOS,  $\rho_s(\mathbf{r}, E)$ , in Eq. (6a) and the barrier transparency coefficient,  $T(\mathbf{r}, E, V)$ , in Eq. (3a):

$$g = \frac{g_e - g_p}{g_e + g_p}, f = \frac{\Delta}{|\phi|}, \varepsilon = \frac{E_s}{\Delta}, \delta = \frac{\Delta}{E_g}, R = \sqrt{Z\phi}, \quad (10)$$

where the dispersion,  $\Delta$ , is dimensionalized on the bulk band gap of MoS<sub>2</sub>,  $E_g = 1.2$  eV.

Parameters in Eq. (10) have a simple physical meaning. Parameter  $g$  determines the ratio of the electron-to-hole states and varies from  $-1$  to  $1$ . Parameter  $f$  is the ratio of the sample LDOS halfwidth to the energy factor,  $|\phi|$ , in the transparency,  $T(\mathbf{r}, E, V)$ . Parameter  $\varepsilon$  is the ratio of the electron or hole LDOS maximum to its halfwidth. Parameter  $\delta$  is the ratio of the electron or hole LDOS halfwidth to the bulk band gap of MoS<sub>2</sub>. Parameter  $R$  is proportional to the STM tip-surface separation,  $d$ . Since the parameter  $R$  determines the exponential factor in  $T(\mathbf{r}, E, V)$ , its values cannot be very small; otherwise, the tunneling current,  $I(\mathbf{r}, V)$ , vanishes. In addition, it cannot be very small, because STM operates in the tunneling regime. The range 0.5–5 appears to be optimal. Using Eq. (10), one could rewrite Eq. (8) for the dimensionless variables, as listed in Appendix C in the Supplemental Material [27], and then determine the LDOS parameters numerically.

The dependences of the dimensionless parameters  $g, f, \varepsilon$ , and  $\delta$  on parameter  $R$  are calculated for HOPG and single-, two-, and three-layer MoS<sub>2</sub> are shown in Fig. 5. The left column corresponds to the forward run, and right column corresponds to the backward run of local  $I$ - $V$  curves of MoS<sub>2</sub> on HOPG substrate, as shown in Fig. 3. The dependences of  $g(R), f(R), \varepsilon(R)$ , and  $\delta(R)$  are very similar, for both the forward and backward runs. Parameters  $g, \delta$ , and  $f$  strongly, and monotonically, increase with an increase in  $R$  for HOPG and three-layer MoS<sub>2</sub>, while their dependences on  $R$  are weaker for two layers and weakest for single-layer MoS<sub>2</sub> (see blue curves in Fig. 5). The parameter  $\varepsilon$  very weakly decreases with an increase in  $R$  for HOPG and single-layer and three-layer MoS<sub>2</sub> (see black curves in Fig. 5). The reduction of  $\varepsilon(R)$  with an increase in  $R$  is stronger for two-layer MoS<sub>2</sub>, but only starts at  $R > 1$ .

Notably, the dependences of  $g(R), f(R), \varepsilon(R)$ , and  $\delta(R)$ , shown in Fig. 5, were obtained from the numerical solution of Eq. (8) in the range of  $0 \leq R \leq 10$ . It appears that positive solutions, which have a physical meaning, exist over a narrower range of  $R$ , namely, for  $0.1 \leq R \leq 5$ , which is shown in Fig. 5. Since the dependences of  $g(R), \varepsilon(R)$ , and  $\delta(R)$  are monotonic and unambiguous functions of  $R$ , the LDOS parameters can be uniquely defined for a fixed  $R$ . In reality, the parameter  $R$  is often unknown due to the uncertainty of the Fermi quasi-level,  $E_F$ , and tip-surface separation,  $d$ . Therefore, probabilistic methods should be used for LDOS reconstruction.

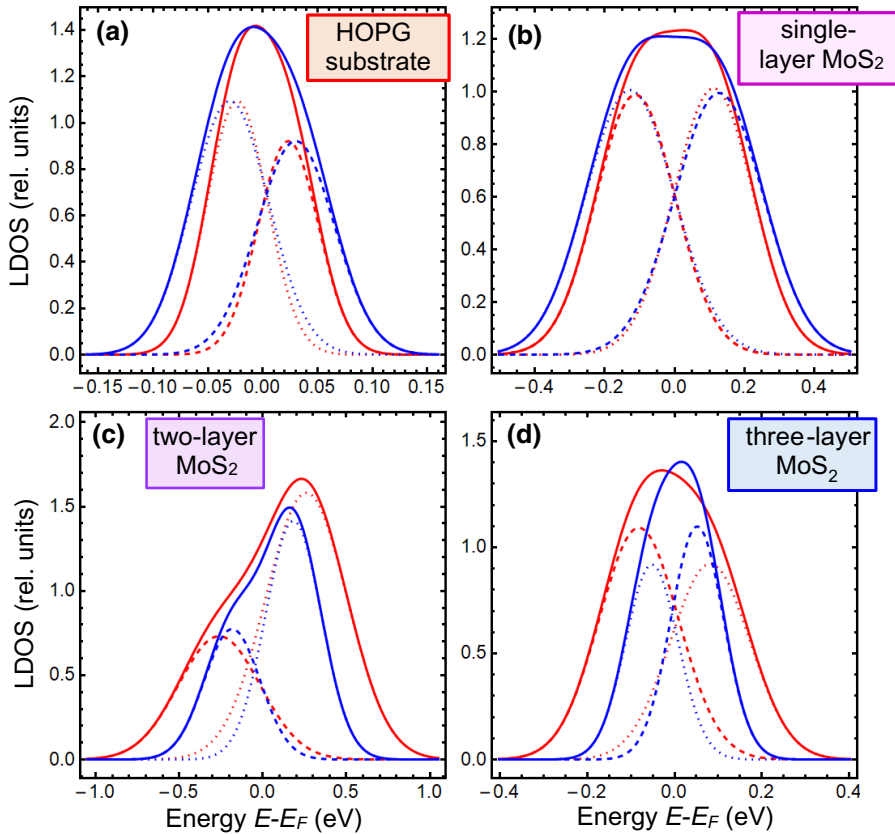


FIG. 6. Reconstructed LDOS for HOPG substrate (a) and single- (b), two- (c), and three-layered (d) MoS<sub>2</sub> nanoflakes on the substrate. Red solid curves correspond to the forward direction, and blue solid curves correspond to the backward direction of local  $I$ - $V$  curves, as shown in Fig. 3. Parameter  $R = 1$ . Dashed and dotted curves show the contribution of two Gaussians to the solid curves.

Reconstructed LDOS for the HOPG substrate and single-, two-, and three-layer MoS<sub>2</sub> nanoflakes are shown in Fig. 6 as solid curves for  $R = 1$ . The red curves correspond to the forward direction and blue curves to the backward direction of local  $I$ - $V$  curves, as shown in Fig. 3. The LDOS reconstructed from the forward and backward runs are very similar for the HOPG substrate and single-layer and three-layer nanoflakes. The LDOS for two-layer nanoflakes are a bit wider for the forward run. As one sees from the dashed and dotted curves, which are the expansions of the solid curves, all reconstructed LDOS significantly differ from a single Gaussian and are well described by two of them.

The thinnest LDOS corresponds to the HOPG substrate; the LDOS of a three-layer MoS<sub>2</sub> nanoflake is at least 2 times wider, the LDOS of a single-layer MoS<sub>2</sub> nanoflake is about 5 times wider, and the LDOS of a two-layer MoS<sub>2</sub> nanoflake is the widest. The LDOS for the HOPG substrate and the three-layer MoS<sub>2</sub> nanoflake have a gaussoïd form with a maximum near  $E = E_F$  [see Fig. 6(a) and 6(d)], while the LDOS of single-layer, and especially two-layer, MoS<sub>2</sub> nanoflakes consists of two gaussoïds, which are inseparable for a single layer and separable for two layers [compare Fig. 6(b) and 6(c)].

The unusual form of the reconstructed LDOS can be explained by the fact that they correspond to strongly corrugated nanoflakes, like that shown in Fig. 1(c). Specifically, the joint action of the size effect and corrugation can lead to a strong modulation of the free carrier density in  $MX_2$  nanoflakes [4,17]. This conclusion is supported by the variability and multiple jumps in the local  $I$ - $V$  characteristics of a STM-probe–sample contact (see Fig. 3), which reflect the randomness of a particular path of tunneling current associated with the local inhomogeneity of electrical conductivity near the surface of MoS<sub>2</sub> nanoflakes, most likely caused by changes to the nanoflake shape and dynamic deformations during flow of the current.

#### IV. CONCLUSIONS

Using a serial expansion of the Tersoff formulas, we propose a flexible method to reconstruct the LDOS from local current-voltage characteristics measured in STM experiments. We establish a set of key physical parameters, which characterize the tunneling current of a STM-probe–sample contact and the sample LDOS expanded in Gaussian functions. Using a direct variational method, coupled with probabilistic analysis, we determine these parameters from the STM experiments for MoS<sub>2</sub> nanoflakes with different numbers of layers. Three case studies are used, a proper semiconductor, a semimetal-type overlapping hole and electron LDOS, and a metallic LDOS.

From the fitting of the  $I$ - $V$  characteristics for different thicknesses of MoS<sub>2</sub> nanoflakes, we determine the LDOS parameters and use the interpolation function describing changes to these parameters with continuous thickening of the MoS<sub>2</sub> layer. The reconstructed LDOS reveal pronounced size effects for the single-layer, two-layer, and three-layer MoS<sub>2</sub> nanoflakes, which we relate to the low dimensionality and strong bending or corrugation of the nanoflakes. This conclusion is supported by the variability and multiple jumps in the local  $I$ - $V$  characteristics of a STM-probe–sample contact, which reflect the randomness of a particular path of tunneling current associated with the local inhomogeneity of electrical conductivity near the surface of the MoS<sub>2</sub> nanoflakes, most likely caused by changes to the nanoflake shape and their dynamic deformations during flow of the current.

The main result of the work is the reconstruction of the LDOS over a relatively wide energy range around the Fermi level, which allows us to gain an insight into the local band structure of LDTMDs. It is calculated in a range of 0.5 V from the Fermi level and the results reveal that the full width at half height of the LDOS is maximal for two-layer MoS<sub>2</sub>, and it begins to decrease for thicker nanoflakes. The unusual forms of the reconstructed LDOS can be explained by the fact that they correspond to strongly corrugated nanoflakes. Specifically, the joint action of the size effect and corrugation can lead to strong modulation of the free carrier density in  $MX_2$  nanoflakes.

The proposed elaboration of the Tersoff approach, allowing LDOS reconstruction, is suitable for a quantitative description of versatile STM experiments, and the obtained results can be useful for a microscopic physical understanding of the surface, strain, and bending contributions to the LDTMDs' electronic properties.

#### V. SAMPLE PREPARATION AND STM MEASUREMENT TECHNIQUES

To characterize the structure of MoS<sub>2</sub> nanoflakes by STM, physisorbed two-dimensional MoS<sub>2</sub> nanoflakes are deposited on the surface from a solution in *n*-tetradecane (C<sub>14</sub>H<sub>30</sub>). To do this, a drop of solution is applied to a freshly made substrate of highly oriented pyrolytic graphite (HOPG). Scanning of the samples is performed under nonvacuum conditions, varying the scan parameters. The probes are made by the mechanical sharpening of Pt-Ir (80:20) wire with a diameter of 0.25 mm. Typical scanning parameters are a voltage of  $U_t = 0.5\text{--}1.8$  V and a current of  $I_t = 50\text{--}200$  pA. Scanning speed varies from 0.1 to 3  $\mu\text{m}/\text{s}$ . The STM images are obtained in dc mode. Local  $I$ - $V$  characteristics are measured with open feedback and locked scanning. SEM images of MoS<sub>2</sub> nanoflakes are obtained on a conductive gold substrate and formed by secondary electrons in a Tescan Vega 3 SBH EasyProbe scanning electron microscope. The sample has the form of

a thin crystal with a complex shape deformed by stresses. The thickness is about 1–3 layers, arranged randomly. For elemental analysis, a Bruker Quantax 610M spectrometer is used and shows the presence of Mo, S, and Cu and O impurities in trace quantities.

## DATA AVAILABILITY

Data supporting reported results was visualized in Mathematica 12.2 [34] and can be found at the Notebook Archive [32].

## ACKNOWLEDGMENTS

A.N.M. and G.I.D. are very grateful to Professor Victor Vainberg, Professor Alexander Marchenko and the referees for useful discussions and valuable suggestions. This work (H.V.S., Y.Yu.L., and G.I.D.) is supported by the National Research Fund of Ukraine (project “Low-dimensional graphene-like transition-metal dichalcogenides with controllable polar and electronic properties for advanced nanoelectronics and biomedical applications,” Grant No. 2020.02/0027). Work by A.N.M. is currently supported by the National Academy of Sciences of Ukraine. This effort is based upon work supported by the U.S. Department of Energy, Office of Science, Office of Basic Energy Sciences Energy Frontier Research Centers program, under Award No. DE-SC0021118 (S.V.K.). Research by Y.K. is supported by the National Research Foundation of Korea (NRF) funded by the Korean government (MSIT) (Grant No. NRF-2021R1A2C2009642).

A.N.M. generated the research idea, formulated the problem, performed analytical calculations (assisted by M.Ye. and E.A.E.), interpreted theoretical and experimental results, and wrote the manuscript draft. H.V.S. performed the mathematical treatment of STM results obtained by Y.Yu.L. E.A.E. performed the fitting and prepared the figures. G.I.D. and M.V.O. prepared the samples and performed SEM measurements. G.S.S., Y.K., and S.V.K. worked on improving the manuscript.

The authors declare no conflict of interest.

- [1] H. J. W. Zandvliet and A. van Houselt, Scanning tunneling spectroscopy, *Annu. Rev. Anal. Chem.* **2**, 37 (2009).
- [2] J. Berry, S. Zhou, J. Han, D. J. Srolovitz, and M. P. Haataja, Dynamic phase engineering of bendable transition metal dichalcogenide monolayers, *Nano Lett.* **17**, 2473 (2017).
- [3] J. Berry, S. Zhou, J. Han, D. J. Srolovitz, and M. P. Haataja, Domain morphology and mechanics of the H/T' transition metal dichalcogenide monolayers, *Phys. Rev. Mater.* **2**, 114002 (2018).

- [4] S. Kang, S. Kim, S. Jeon, W.-S. Jang, D. Seol, Y.-M. Kim, J. Lee, H. Yang, and Y. Kim, Atomic-scale symmetry breaking for out-of-plane piezoelectricity in two-dimensional transition metal dichalcogenides, *Nano Energy* **58**, 57 (2019).
- [5] R. Grasset, Y. Gallais, A. Sacuto, M. Cazayous, S. Mañas-Valero, E. Coronado, and M.-A. Méasson, Pressure-Induced Collapse of the Charge Density Wave and Higgs Mode Visibility in 2 H–TaS<sub>2</sub>, *Phys. Rev. Lett.* **122**, 127001 (2019).
- [6] Y. Qi, W. Shi, P. G. Naumov, N. Kumar, R. Sankar, W. Schnelle, C. Shekhar, F. C. Chou, C. Felser, B. Yan, and S. A. Medvedev, Topological quantum phase transition and superconductivity induced by pressure in the bismuth tellurohalide BiTeI, *Adv. Mater.* **29**, 1605965 (2017).
- [7] L. Dong, J. Lou, and V. B. Shenoy, Large in-plane and vertical piezoelectricity in Janus transition metal dichalcogenides, *ACS Nano* **11**, 8242 (2017).
- [8] A. N. Morozovska, E. A. Eliseev, K. D. Stubbs, R. Vasudevan, Y. Kim, and S. V. Kalinin, Phase diagrams of single layer two-dimensional transition metal dichalcogenides: Landau theory, *Phys. Rev. B* **101**, 195424 (2020).
- [9] R. K. Vasudevan, M. Ziatdinov, L. Vlcek, A. N. Morozovska, E. A. Eliseev, Shi-Ze Yang, Y. Gong, P. Ajayan, W. Zhou, M. F. Chisholm, and S. V. Kalinin, Investigating phase transitions from local crystallographic analysis based on statistical learning of atomic environments in 2D MoS<sub>2</sub>-ReS<sub>2</sub>, *Appl. Phys. Rev.* **8**, 011409 (2021).
- [10] V. Sanchez, E. Benavente, V. Lavayen, C. O’Dwyer, C. M. Sotomayor-Torres, G. González, and M. A. Santa Ana, Pressure induced anisotropy of electrical conductivity in polycrystalline molybdenum disulfide, *Appl. Surf. Sci.* **252**, 7941 (2006).
- [11] Jun Suk Kim, Jaesu Kim, Jiong Zhao, Sungho Kim, Jin Hee Lee, Youngjo Jin, Homin Choi, Byoung Hee Moon, Jung Jun Bae, Young Hee Lee, and Seong Chu Lim, Electrical transport properties of polymorphic MoS<sub>2</sub>, *ACS Nano* **10**, 7500 (2016).
- [12] Wei-Chu Shen, Ruei-San Chen, and Ying-Sheng Huang, Photoconductivities in MoS<sub>2</sub> nanoflake photoconductors, *Nanoscale Res. Lett.* **11**, 124 (2016).
- [13] A. Grillo, F. Giubileo, L. Iemmo, G. Luongo, F. Urban, and A. Di Bartolomeo, Space charge limited current and photoconductive effect in few-layer MoS<sub>2</sub>, *J. Phys.: Conf. Ser.* **1226**, 012013 (2019).
- [14] Jorge Quereda, Juan José Palacios, Nicolás Agrait, Andres Castellanos-Gomez, and Gabino Rubio-Bollinger, Strain engineering of Schottky barriers in single- and few-layer MoS<sub>2</sub> vertical devices, *2D Mater.* **4**, 021006 (2017).
- [15] Ashby Phillip John, Arya Thenapparambi, and Madhu Thalakulam, Strain-engineering the Schottky barrier and electrical transport on MoS<sub>2</sub>. <https://arxiv.org/abs/2004.05061v1>
- [16] Shun-Tsung Lo, O. Klochan, C.-H. Liu, W.-H. Wang, A. R. Hamilton, and C.-T. Liang, Transport in disordered monolayer MoS<sub>2</sub> nanoflakes—evidence for inhomogeneous charge transport, *Nanotechnology* **25**, 375201 (2014).
- [17] A. N. Morozovska, E. A. Eliseev, G. I. Dovbeshko, M. D. Glinchuk, Y. Kim, and S. V. Kalinin, Flexo-induced

- ferroelectricity in low dimensional transition metal dichalcogenides, *Phys. Rev. B* **102**, 075417 (2020).
- [18] A. N. Morozovska, E. A. Eliseev, H. V. Shevliakova, Y. Yu. Lopatina, G. I. Dovbeshko, M. D. Glinchuk, Y. Kim, and S. V. Kalinin, Correlation between Corrugation-Induced Flexoelectric Polarization and Conductivity of Low-Dimensional Transition Metal Dichalcogenides, *Phys. Rev. Appl.* **15**, 044051 (2021).
- [19] H. V. Shevliakova, S. O. Yesylevskyy, I. Kupchak, G. I. Dovbeshko, Y. Kim, and A. N. Morozovska, Flexoelectric and piezoelectric coupling in a bended MoS<sub>2</sub> monolayer, *Symmetry* **13**, 2086 (2021).
- [20] J. G. Simmons, Generalized formula for the electric tunnel effect between similar electrodes separated by a thin insulating film, *J. Appl. Phys.* **34**, 1793 (1963).
- [21] J. G. Simmons, Electric tunnel effect between dissimilar electrodes separated by a thin insulating film, *J. Appl. Phys.* **34**, 2581 (1963).
- [22] J. Tersoff and Donald R. Hamann, Theory of the scanning tunneling microscope, *Phys. Rev. B* **31**, 805 (1985).
- [23] P. Zhang, Scaling for quantum tunneling current in nano- and subnano-scale plasmonic junctions, *Sci. Rep.* **5**, 9826 (2015).
- [24] B. Koslowski, Ch Dietrich, A. Tschetschetkin, and P. Ziemann, Evaluation of scanning tunneling spectroscopy data: Approaching a quantitative determination of the electronic density of states, *Phys. Rev. B* **75**, 035421 (2007).
- [25] M. Passoni, F. Donati, A. Li Bassi, C. S. Casari, and C. E. Bottani, Recovery of local density of states using scanning tunneling spectroscopy, *Phys. Rev. B* **79**, 045404 (2009).
- [26] Krisztián Palotás, Gábor Mándi, and Werner A. Hofer, Three-dimensional Wentzel-Kramers-Brillouin approach for the simulation of scanning tunneling microscopy and spectroscopy, *Front. Phys.* **9**, 711 (2014).
- [27] See the Supplemental Material at <http://link.aps.org supplemental/10.1103/PhysRevApplied.17.064037> for details of calculations and additional figure.
- [28] A. Kuc, N. Zibouche, and T. Heine, Influence of quantum confinement on the electronic structure of the transition metal sulfide TS2, *Phys. Rev. B* **83**, 245213 (2011).
- [29] J. A. Kubby and J. J. Boland, Scanning tunneling microscopy of semiconductor surfaces, *Surf. Sci. Rep.* **26**, 61 (1996).
- [30] H. Oka, O. O. Brovko, M. Corbetta, V. S. Stepanyuk, D. Sander, and J. Kirschner, Spin-polarized quantum confinement in nanostructures: Scanning tunneling microscopy, *Rev. Mod. Phys.* **86**, 1127 (2014).
- [31] S. V. Kalinin, S. Jesse, B. J. Rodriguez, E. A. Eliseev, V. Gopalan, and A. N. Morozovska, Quantitative Determination of Tip Parameters in Piezoresponse Force Microscopy, *Appl. Phys. Lett.* **90**, 212905 (2007).
- [32] See Mathbook in Notebook Archive. <https://notebook archive.org/2022-01-debqm3r>
- [33] Christopher T. Nelson, Rama K. Vasudevan, Xiaohang Zhang, Maxim Ziatdinov, Eugene A. Eliseev, Ichiro Takeuchi, Anna N. Morozovska, and Sergei V. Kalinin, Exploring physics of ferroelectric domain walls via Bayesian analysis of atomically resolved STEM data, *Nat. Commun.* **11**, 6361 (2020).
- [34] <https://www.wolfram.com/mathematica>